Modeling of HMX/GAP Pseudo-Propellant Combustion

E. S. KIM and V. YANG*
Department of Mechanical and Nuclear Engineering, The Pennsylvania State University, University Park, PA 16802, USA

and

Y.-C. LIAU
Chemical Science and Technology Division, Los Alamos National Laboratory, Los Alamos, NM 87545, USA

A comprehensive numerical analysis of HMX/GAP pseudo-propellant combustion has been established to predict the propellant burning rate and detailed combustion wave structure over a broad range of ambient pressure, laser intensity, and propellant composition. The model takes into account various fundamental processes at scales sufficient to resolve the microscopic flame-zone physiochemistry. The thermochemical parameters of HMX and GAP are deduced from existing experimental data. Four global decomposition reactions of HMX and GAP in the condensed phase as well as subsequent reactions are included. In the gas phase, a detailed chemical kinetics scheme involving 74 species and 532 reactions is employed to describe the heat-release mechanism. The effect of the external CO_2 laser on the propellant burning characteristics prevails at low pressures, but decreases at high pressures at which the conductive heat feedback from the gaseous flame to the condensed phase overrides surface absorption of radiation energy. The burning rate decreases with the addition of GAP at low pressures, even though GAP burns much faster than pure HMX. One factor contributing to this phenomenon is the rapid gasification of GAP displacing the primary flame away from the surface. Conversely, above a certain pressure level, the burning rate may be considerably enhanced by adding a small amount of GAP because of the higher surface temperature at which the exothermic decomposition of GAP plays a decisive role in providing energy to sustain propellant burning. © 2002 by The Combustion Institute

NOMENCALTURE

A	cross-sectional area of propellant sample
A_g	fractional cross-sectional area consisting of gas bubbles in two-phase region
A_j	pre-exponential factor of rate constant of reaction j
A_s	interface area between bubbles and liquid per unit volume
a	pre-exponential factor of burning-rate law
B_j	temperature exponent in rate constant of reaction j
C_i	molar concentration of species i
c_{pi}	constant-pressure specific heat of species i
E_j	activation energy of reaction j
e	internal energy
H_v	enthalpy of vaporization
h	enthalpy
h_c	heat transfer coefficient
h_i	static enthalpy of species i
$h^\circ_{f_i}$	heat of formation of species i at standard condition
k_j	rate constant of reaction j
$\dot{m}''$	mass flux
N	total number of species
n	pressure exponent
N_R	total number of reactions
p	pressure
p_0	pre-exponential factor of vapor pressure in Arrhenius form
r_b	propellant burning rate
R_u	universal gas constant
T	temperature
s	sticking coefficient
t	time
u	bulk velocity
V_i	diffusion velocity of species i
$\bar{v}_n$	average normal velocity component of vapor molecule
W_i	molecular weight of species i
$\dot{w}_i$	mass production rate of species i
$\dot{w}_{Rj}$	mass production rate of reaction j

---

*Corresponding author. E-mail: vigor@psu.edu

COMBUSTION AND FLAME 131:227–245 (2002)

Published by Elsevier Science Inc.

0010-2180/02/$–see front matter
PII S0010-2180(02)00411-X

X_i	molar fraction of species *i*
x	spatial coordinate
Y_i	mass fraction of species *i*

Greek symbols

ϕ	void fraction
ρ	density
λ	thermal conductivity
$\dot{\omega}$	molar production rate

Subscripts

0^+	gas-phase side of propellant surface
0^-	condensed-phase side of propellant surface
c	condensed phase
c–g	from condensed to gas phase
cond	condensation
eq	equilibrium condition
evap	evaporation
f	mass-averaged quantity in subsurface foam layer
g	gas phase
i	preconditioned state
l	liquid phase
s	propellant surface or solid phase
v	vapor

INTRODUCTION

This paper deals with the theoretical modeling and numerical simulation of steady-state combustion of cyclotetramethylenetetranitramine (HMX)/glycidyl azide polymer (GAP) pseudo-propellants. The prefix pseudo is used to emphasize that HMX and GAP are mixed physically and no curing agent is used as for operational propellants. These two energetic compounds, with their molecular structures shown in Fig. 1, have been widely used in many propulsion and gas-generation systems to meet various stringent performance and environmental requirements. In the past decade, significant progress has been made in the study of combustion-wave structures and burning characteristics of nitramine monopropellants such as cyclotrimethylenetrinitramine (RDX) and HMX. Extensive experimental diagnostics [1–3] and theoretical analyses [4–11] were conducted over a broad range of operating conditions. Both self-sustained and laser-assisted combustion [4–10], as well as ignition transients [11], have been treated in detail. A comprehensive summary of the latest developments is covered in a volume edited by Yang et al. [12].

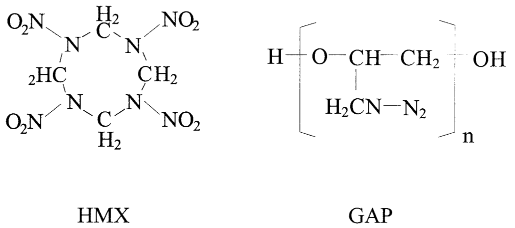

Fig. 1. Molecular structures of HMX and GAP.

Unlike the situation with nitramine monopropellants, detailed theoretical modeling of GAP decomposition and combustion has not yet been conducted, although some initial attempts were made recently based on global decomposition pathways [13–14]. Much effort, however, has been expended on experimental studies [3, 15–21]. The physiochemical processes involved in the combustion of a cured GAP strand is schematically illustrated in Fig. 2. The entire combustion-wave structure can be segmented into three regions: solid-phase, near-surface two phase, and gas-phase regimes. In the solid phase, the extent of chemical reactions is usually negligible due to the low temperature and short residence time. Thermal decomposition and ensued reactions, as well as phase transition, take place in the foam layer, generating gas bubbles and forming a two-phase region. Rapid gasification occurs at the burning surface, and further decomposition and oxidation continue to take place and release a significant amount of energy in the near-surface region. The burning surface temperature is greater than 700 K. No visible flame is observed in the gas phase; instead, a large amount of fine powder is formed away from the burning surface and generates a cloud of intense smoke. The final flame temperature of GAP is around 1300 to 1500 K, which is significantly lower than those of nitramines (~3000 K).

Recently, gas-phase species and temperature measurements were conducted to investigate CO_2 laser-induced pyrolysis of cured GAP at the intensities of 100 and 200 W/cm^2 under atmospheric pressure using a triple quadrupole

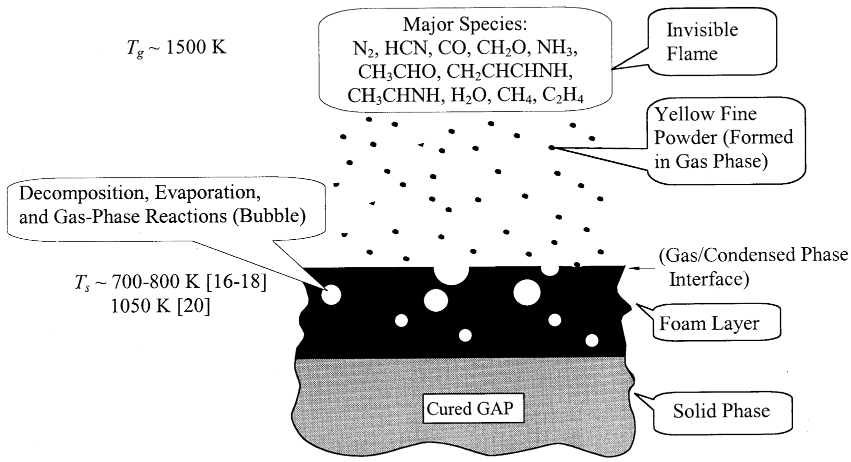

Fig. 2. Combustion-wave structure of GAP.

mass spectrometer (TQMS) with fine-wire thermocouples [20]. The decomposition products observed in that work were N_2 HCN, CO, H_2CO, NH_3, CH_3CHO, $CH_2CHCHNH$, CH_3CHNH, H_2O, CH_4 and C_2H_4. Among these, the major species were N_2, HCN, CO, and H_2CO. The relative concentrations of these decomposed species were similar to those observed by Arisawa and Brill [19]. Very intense smoke was formed in the gas phase; no carbonaceous residue was observed on the burning surface. The smoke formation was thus assumed to be caused by cold ambient gases, quenching hot condensable gases issuing from the GAP surface. The surface temperature was measured to be 1050 K under both heat fluxes of 100 and 200 W/cm^2, which is considerably higher than those reported in the literature (T_s = 700–760 K [17], 710–750 K [18], and 813 K [16]) due to differences in sample preparation (cured vs. uncured GAP), experimental conditions (self-sustained vs. laser-assisted combustion), type of GAP strands used, diagnostic technique, and measurement accuracy. Both the surface temperature and the burning rate of GAP were higher than those of HMX under the same experimental condition.

The T-jump/FTIR spectroscopy technique was applied to the study of the decomposition characteristics of GAP having one, two, and three terminal -OH groups [19]. Samples were rapidly heated to a temperature range of 500 to 600 K at 2 atm with a heating rate of 800 K/s. The major decomposition products were CH_4, HCN, CO, C_2H_4, NH_3, CH_2O, CH_2CO, H_2O, and GAP oligomer. IR-inactive N_2 was not measured, but is present as one of the major decomposition products of GAP in other studies using mass spectrometry [15, 20]. NH_3 was found to be formed from the end chain of the azide group. The formation of CO appeared to result from both the parent polymer and secondary reactions. The ratio of HCN to NH_3 increased as temperature increased. The intensive heat release during GAP decomposition explains the high burning surface temperature of GAP [20].

By using TQMS with fine-wire thermocouples, Litzinger et al. [3] conducted gas-phase species and temperature measurements to study the combustion characteristics of several nitramine/azide pseudo-propellants including RDX/GAP and HMX/GAP, all with a mass ratio of 8:2. The experiments were performed at CO_2 laser heat fluxes of 100-400 W/cm^2 under atmospheric pressure. Emphasis was placed on the effects of nitramine/azide interaction and external heat flux. The major decomposition species for HMX/GAP and RDX/GAP were similar to those found for neat HMX and RDX. The species-concentration profiles showed three distinct regions: a primary reaction zone, a dark zone, and a secondary reaction zone. The burning rates of HMX/GAP and RDX/GAP were increased with the addition of GAP, regardless of the laser energy intensity impressed. This

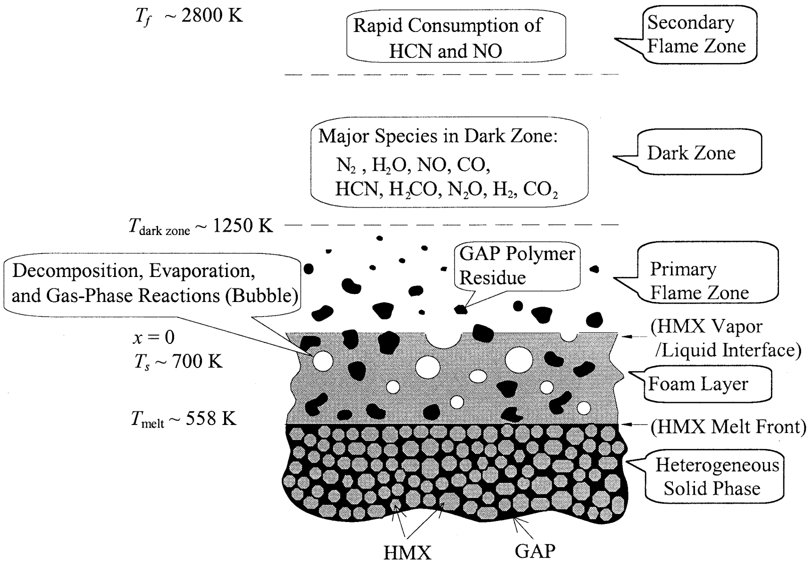

Fig. 3. Combustion-wave structure of HMX/GAP pseudo-propellant at 1 atm.

finding contradicted the experimental results obtained by Kubota and Sonobe [17], which showed that the addition of GAP into HMX lowered the burning rate. The discrepancy may arise from the differences in their experimental setups and sample preparation. For instance, the HMX used by Kubota and Sonobe [17] had a bimodal particle size distribution (70% of 2 μm and 30% of 20 μm), compared with an average crystal size of 75 μm used by Litzinger et al. [3]. Furthermore, the GAP was cured with hexamethylene diisocyanate (HMDI) and crosslinked with trimethylolpropane (TMP) in Kubota and Sonobe's experiments.

Recently, modeling of RDX/GAP pseudo-propellant combustion was performed by Liau et al. [13]. Four global decomposition reactions of RDX and GAP, as well as subsequent reactions, were considered in the condensed phase. In the gas phase, a chemical kinetics scheme containing 71 species and 520 reactions was employed to study the detailed heat release mechanism. The model was applied to a broad range of pressure and laser intensity with various GAP concentrations. Reasonably good agreement was achieved with experimental data on burning rate and species concentration profiles at CO_2 laser fluxes of 100 and 300 W/cm^2 under atmospheric pressure. The burning rate could be either increased or decreased with the addition of GAP, depending on the laser heat flux.

The present work extends an existing model for the steady-state combustion of RDX/GAP pseudo-propellants [13] to include the salient features of HMX. The objective is to investigate the key physiochemical processes dictating the HMX/GAP propellant burning behavior and flame structure over a broad range of ambient pressure, preconditioned temperature, and impressed laser intensity. The analysis is based on the conservation equations of mass, energy, and species concentration for both the condensed and gas phases, and takes into account finite-rate chemical kinetics and variable thermophysical properties. Results will provide comprehensive insight into the entire combustion-wave structure. The effects of propellant composition on the burning rate, surface temperature, melt-layer thickness, and surface void fraction will be examined systematically.

THEORETICAL FORMULATION

Figure 3 shows schematically the physiochemical processes involved in the HMX/GAP pseudo-propellant combustion. The entire combustion-wave structure is segmented into three regions: solid phase, near-surface two phase,

TABLE 1

Thermodynamic and Transport Properties of HMX and GAP

Parameter	Units	Value	Ref. or Comments
$c_{p,s,\mathrm{HMX}}$	cal/gK	$4.980 \times 10^{-2} + 0.660 \times 10^{-3} \times T$	23
$c_{p,l,\mathrm{HMX}}$	cal/gK	$4.980 \times 10^{-2} + 0.660 \times 10^{-3} \times T$	$c_{p,l,\mathrm{HMX}} = c_{p,s,\mathrm{HMX}}$
$c_{p,l,\mathrm{GAP}}$	cal/gK	$1.503 \times 10^{-1} + 0.966 \times 10^{-3} \times T$	23
$\lambda_{s,\mathrm{HMX}}$	cal/K s cm	$1.500 \times 10^{-3} - 0.115 \times 10^{-5} \times T$	23
$\lambda_{l,\mathrm{HMX}}$	cal/K s cm	$1.500 \times 10^{-3} - 0.115 \times 10^{-5} \times T$	$\lambda_{l,\mathrm{HMX}} = \lambda_{s,\mathrm{HMX}}$
$\lambda_{l,\mathrm{GAP}}$	cal/K s cm	$1.050 \times 10^{-3} - 0.146 \times 10^{-5} \times T$	23
$\rho_{s,\mathrm{HMX}}$	g/cm^3	1.9	24
$\rho_{l,\mathrm{HMX}}$	g/cm^3	1.9	$\rho_{s,\mathrm{HMX}} = \rho_{l,\mathrm{HMX}}$
$\rho_{l,\mathrm{GAP}}$	g/cm^3	1.3	19
$T_{\delta \rightarrow l,\mathrm{HMX}}$	K	558	24
$T_{\beta \rightarrow \delta,\mathrm{HMX}}$	K	460	6
$H_{v,\mathrm{HMX}}$	kcal/mol	38.7	34
$H_{\delta \rightarrow l,\mathrm{HMX}}$	kcal/mol	16.7	25
$H_{\beta \rightarrow \delta,\mathrm{HMX}}$	kcal/mol	2.35	26

and gas phase. In the solid-phase region, HMX powder and GAP are physically mixed. The former melts at 558 K with negligible chemical reactions taking place, due to the low temperature and short residence time. Thermal decomposition and phase change of HMX occurs in the liquid phase to form a foam layer. The propellant surface (x = 0) is defined herein as the interface between the foam layer and gas-phase region, at which rapid gasification of HMX prevails. Because the surface temperature of HMX/GAP pseudo-propellant (~700 K) is lower than that of pure GAP, GAP leaves the surface as aerosol surrounded with vapor HMX and its decomposed gaseous products. In this region, GAP remains as a condensed species and continues to decompose. A significant amount of carbonaceous residue may be present on the surface during combustion.

To facilitate analysis, the coordinate system is fixed at the propellant surface. A quasi one-dimensional model is formulated as a first approximation of the problem. Both the subsurface and gas-phase regions require a multiphase treatment because of the presence of GAP and other condensed species in these zones. A detailed derivation of the theoretical model is available in Ref. 22. It may be described briefly as follows.

Solid-Phase Region

Thermal decomposition of HMX and GAP and in-depth radiation absorption are ignored in modeling the solid-phase process. Thus, only heat conduction governed by the following equation is considered:

$$\rho_c c_c \frac{\partial T_c}{\partial t} + \rho_c u_c c_c \frac{\partial T_c}{\partial x} = \frac{\partial}{\partial x}\left(\lambda_c \frac{\partial T_c}{\partial x}\right) \tag{1}$$

The thermal conductivities and specific heat capacities of solid HMX and liquid GAP were recently obtained as a function of temperature by Hanson-Parr and Parr [23]. Measurements of these properties for liquid HMX, however, represent a much more challenging task, because decomposition usually takes place before the melting. Thus, they are assumed to be identical to those at the solid state due to the lack of reliable data. The thermodynamic and transport properties used in the present work are given in Table 1. The properties of the mixture are estimated as follows.

$$\rho_c c_c = Y_{\mathrm{HMX}} \rho_{\mathrm{HMX}} c_{\mathrm{HMX}} + Y_{\mathrm{GAP}} \rho_{\mathrm{GAP}} c_{\mathrm{GAP}} \tag{2}$$

$$\lambda_c = Y_{\mathrm{HMX}} \lambda_{\mathrm{HMX}} + Y_{\mathrm{GAP}} \lambda_{\mathrm{GAP}} \tag{3}$$

A closed-form solution to Eq. 1 at steady state is available subject to appropriate boundary conditions and the propellant burning rate.

Subsurface Multi-Phase Region

The physiochemical processes in this region are extremely complex, involving an array of intricacies such as thermal decomposition, evaporation, bubble formation, gas-phase reactions in bubbles, and interfacial transport of mass and energy between the gas and condensed phases. A two-phase fluid dynamic model based on a spatial averaging technique is employed to formulate these complicated phenomena [5]. With the assumption that mass diffusion is negligible, the conservation equations for both the condensed and gas phases can be combined and written as follows.

Mass

$$\frac{\partial[(1-\phi_f)\rho_c+\phi_f\rho_g]}{\partial t}+\frac{\partial}{\partial x}[(1-\phi_f)\rho_c u_c+\phi_f\rho_g u_c+\phi_f\rho_g u_g]=0, \tag{4}$$

Condensed species concentration

$$\frac{\partial[1-\phi_f)\rho_c Y_{c_i}]}{\partial t}+\frac{\partial}{\partial x}[(1-\phi_f)\rho_c u_c Y_{c_i}] = \dot{w}_{c_i} \quad (i=1,2,\ldots,N_c), \tag{5}$$

Gaseous species concentration

$$\frac{\partial(\phi_f\rho_g Y_{g_i})}{\partial t}+\frac{\partial(\phi_f\rho_g u_g Y_{g_i})}{\partial x}=\dot{w}_{g_i} \quad (i=1,2,\ldots,N_g), \tag{6}$$

Energy

$$\rho_f c_f\frac{\partial T_f}{\partial t}-\frac{\partial p}{\partial t}+\rho_f u_f c_f\frac{\partial T_f}{\partial x}=\frac{\partial}{\partial x}\left(\lambda_f\frac{\partial T_f}{\partial x}\right) - \sum_{j=1}^{N_g}\dot{w}_{gj}h_{gj}-\sum_{j=1}^{N_g}\dot{w}_{cj}h_{cj} + \sum_{j=1}^{N_g}h_{gj}Y_{gj}\dot{w}_{c\text{–}g}-\sum_{j=1}^{N_c}h_{cj}Y_{cj}\dot{w}_{c\text{–}g} \tag{7}$$

where $\dot{w}_{c\text{–}g}$ represents the rate of mass conversion from liquid to gas. The properties are mass-averaged as follows.

$$\rho_f c_f=(1-\phi_f)\rho_c c_c+\phi_f\rho_g c_g, \tag{8}$$

$$\rho_f u_f c_f = (1-\phi_f)\rho_c u_c c_c+\phi_f\rho_g u_g c_g, \tag{9}$$

$$\lambda_f=[(1-\phi_f)\rho_c u_c\lambda_c+\phi_f\rho_g u_g\lambda_g]/[(1-\phi_f)\rho_c u_c+\phi_f\rho_g u_g] \tag{10}$$

where

$$c_c=\sum_{i=1}^{N_c}c_{c_i}Y_{c_i},\ c_g=\sum_{i=1}^{N_g}c_{g_i}Y_{g_i},$$

$$\lambda_c=\sum_{i=1}^{N_c}\lambda_{c_i}Y_{c_i},\ \text{and}\ \lambda_g=\sum_{i=1}^{N_g}\lambda_{g_i}Y_{g_i} \tag{11a–d}$$

The mass and energy production terms depend on the specific chemical reaction mechanisms used and can be formulated as described below.

The model accommodates the thermal decomposition of HMX and GAP, as well as subsequent reactions in the foam layer. The formation of gas bubbles due to evaporation and thermal degradation is also considered for completeness. Two global-decomposition pathways are employed for HMX, as listed in Table 2. The first reaction (R1) is an exothermic, low-temperature pathway, whereas the second reaction (R2) is an endothermic, high-temperature pathway. Unfortunately, uncertainties still exist about the kinetic rates of (R1) and (R2). Thus, a parametric study is performed to assess the role of the condensed-phase kinetics of HMX in the overall combustion process of HMX/GAP pseudo-propellant. Two different sets of rates are available in the literature for (R1) and (R2): one estimated by Davidson and Beckstead [6] using their combustion model and the other obtained by Brill [27] from the T-jump/FTIR experiment. Subsequent reactions among the products of (R1) and (R2) may occur to provide the thermal energy to sustain pyrolysis. Brill [27] examined several plausible secondary reactions and their reaction rates. Results indicate that reaction (R6) between CH_2O and NO_2 is probably the most important one in the foam layer if it indeed does occur. The rate parameter of reaction (R6) was determined with shock-tube experiments [28]. Thermodynamic phase transition consisting of both evaporation and condensation of HMX, (R5), is considered to provide a complete description of the mass transfer process.

The GAP sample considered in the present study is composed of 56 monomer units and is

TABLE 2

Subsurface Chemical Reactions and Rate Parameters

No.	Reaction	$A^{a,c}$	$E^{b,c}$	Ref.
R1	$HMX_{(l)} \rightarrow 4CH_2O + 4N_2O$	5.81×10^{10}	34,000	6
		1.00×10^{13}	34,400	27
R2	$HMX_{(l)} \rightarrow 4HCN + 2\,(NO_2 + NO + H_2O)$	1.66×10^{14}	44,100	6
		$1.00 \times 10^{16.5}$	44,100	27
R3	$GAP56_{(l)} \rightarrow GAP56^*_{(l)} + 56N_2$	5×10^{15}	41,500	13
R4	$GAP56^*_{(l)} \rightarrow 25.6HCN + 15.8CO + 14.4NH_3 +$ $17.8CH_2O + 16CH_3CHO + H_2O + 6.4C_2H_3CHO +$ $1.5C_2H_4 + 8CH_3CHNH + 8CH_2CHCHNH + 14.6C_{(s)}$	1.28×10^{19}	53,000	13
R5	$HMX_{(l)} \Leftrightarrow HMX_{(g)}$	See Ref. 5	—	13
R6	$CH_2O + NO_2 \rightarrow CO + NO + H_2O$	$802 \times T^{2.77}$	13,730	13
R7	$CH_3CHO + M = CH_3 + HCO + M$	7×10^{15}	81,770	13
R8	$C_2H_3CHO + M = C_2H_3 + HCO + M$	10^{16}	97,600	13
R9	$CH_3CHNH + M = CH_3 + H_2CN + M$	10^{16}	63,700	13
R10	$CH_2CHCHNH + M = C_2H_3 + H_2CN + M$	10^{16}	66,900	13

[a] A = pre-exponential factor; [b] E = activation energy; [c] Units are in mol, cm, s, K, and cal.

denoted "GAP56." A global, condensed-phase decomposition mechanism for GAP was established based on the experimental data reported in [19, 20, 29]. There is universal agreement that GAP decomposition is initiated by the bond cleavage of the azide group releasing N_2 [15–21, 30, 31]. This process proceeds rapidly over a temperature range from 260 to 290°C, and has an activation energy of about 41 kcal/mol [19]. There are, however, uncertainties as to how the bond breaking process occurs. We assume a first-order reaction with the pre-exponential factor and activation energy deduced by Sysak et al. [29], as given by reaction (R3) in Table 2.

The subsequent step in the decomposition of GAP releases NH_3 Its concentration in the gas phase increases with increasing number of -OH end groups in the polymer. It appears that H-atom abstraction involving the -OH end group is an important channel for NH_3 formation. At this time, there are no mechanistic details which allow one to quantify the NH_3 evolution as a global reaction, and thus, a rate expression cannot be formulated. Because NH_3 is an important source for H-atoms in the gas phase, the deficiency in predicted species concentrations caused by neglecting this step in the decomposition of GAP must be noted. Finally, a rapid, highly exothermic event takes place and releases HCN, CO, CH_2O, CH_2CO, CH_4, C_2H_4, H_2O, and GAP oligomers, in addition to NH_3 [19].

In the laser-assisted combustion study of GAP polyol by Tang et al. [20], the surface temperature approached 1050 K, which was about 400 K higher than those treated by Arisawa and Brill [17]. Because of this higher temperature, Tang et al. [20] identified several different large molecular species using TQMS. The major ones were acetaldehyde (CH_3CHO), acrolein (C_2H_3CHO), and different imines (CH_3CHNH and $CH_2CHCHNH$). In comparing the results of Arisawa and Brill [19] with those of Tang et al. [20], it appears that the GAP oligomers identified by Arisawa and Brill are likely candidates to form the imines identified by Tang et al. A species balance of the data acquired by Tang et al. [20] leads to a global reaction model for the decomposition of GAP56*, which is the polymer unit that has released N_2, as given by reaction (R4) in Table 2.

Most of the gaseous decomposition products from GAP are hydrocarbons or common gases whose chemical kinetic details are readily available. However, the available information about aldehydes (CH_3CHO and C_2H_3CHO) and imines (CH_3CHNH and $CH_2CHCHNH$), as well as their interactions with either HMX or its decomposition products, appears to be limited. To allow for a reduction of these species, bimolecular decomposition reactions have been formulated, with the activation energies about the differences in enthalpy between products and reactants [13]. The pre-exponential factors are assigned values that are typical for such a pro-

TABLE 3

Description of Species Formation in Foam Layer

i	Species	$\dot{w}_{c_i}$ or $\dot{w}_{g_i}$
1	$HMX_{(l)}$	$-(\dot{w}_{R1} + \dot{w}_{R2} + \dot{w}_{R5})$
2	$GAP56_{(l)}$	$-\dot{w}_{R3}$
3	$GAP56^*_{(l)}$	$\dot{w}_{R3}W_3/W_2 - \dot{w}_{R4}$
4	$C_{(s)}$	$14.6\dot{w}_{R4}W_4/W_3$
5	$HMX_{(g)}$	$\dot{w}_{R5}$
6	CH_2O	$W_6(3\dot{w}_{R1}/W_1 + 17.8\dot{w}_{R4}/W_3 - \dot{w}_{R6})$
7	N_2O	$W_7(3\dot{w}_{R1}/W_1)$
8	HCN	$W_8(3\dot{w}_{R2}/W_1 + 25.6\dot{w}_{R4}/W_3)$
9	NO_2	$W_9(1.5\dot{w}_{R2}/W_1 - \dot{\omega}_{R6})$
10	NO	$W_{10}(1.5\dot{w}_{R2}/W_1 + \dot{\omega}_{R6})$
11	H_2O	$W_{11}(1.5\dot{w}_{R2}/W_1 + \dot{w}_{R4}/W_3 + \dot{\omega}_{R6})$
12	N_2	$W_{12}(56\dot{w}_{R3}/W_2)$
13	CO	$W_{13}(15.8\dot{w}_{R4}/W_3 + \dot{\omega}_{R6})$
14	NH_3	$W_{14}(14.4\dot{w}_{R4}/W_3)$
15	C_2H_4	$W_{15}(1.5\dot{w}_{R4}/W_3)$
16	CH_3CHO	$W_{16}(16\dot{w}_{R4}/W_3)$
17	C_2H_3CHO	$W_{17}(6.4\dot{w}_{R4}/W_3)$
18	CH_3CHNH	$W_{18}(8\dot{w}_{R4}/W_3)$
19	$CH_2CHCHNH$	$W_{19}(8\dot{w}_{R4}/W_3)$

cess. The reactions considered are listed as reactions (R7-R10) in Table 2.

Note that the condensed species GAP56$_{(l)}$, GAP56*$_{(l)}$, and C$_{(s)}$ are dissolved in liquid HMX, whereas all other species are gaseous and exist in bubbles. Based on the chemical mechanism given by (R1-R6), the species production terms in Eqs. 5 and 6 are listed in Table 3. The forward and backward reactions in (R5) denote the evaporation and condensation processes between liquid and vapor HMX. The production terms for reactions in Table 3 are defined as

$$\dot{w}_{R1} = (1 - \phi_f)\,\rho_c Y_{c,1}\,k_1 \tag{12}$$

$$\dot{w}_{R2} = (1 - \phi_f)\,\rho_c Y_{c,1}\,k_2 \tag{13}$$

$$\dot{w}_{R3} = (1 - \phi_f)\,\rho_c Y_{c,2}\,k_3 \tag{14}$$

$$\dot{w}_{R4} = (1 - \phi_f)\,\rho_c Y_{c,3}\,k_4 \tag{15}$$

$$\begin{aligned}\dot{w}_{R5} &= A_s(k_{5f} - k_{5b})\\ &= A_s s \bar{v}_n C_{\mathrm{RDX}}\left(\frac{P_{v,\mathrm{eq}}}{p} - X_{g,5}\right)\end{aligned} \tag{16}$$

where

$$s = 1 \text{ and } p_{v,\mathrm{eq}} = P_o \exp\left(-\frac{H_v}{R_u T}\right), \tag{17}$$

$$\dot{\omega}_{R6} = \phi_f k_6 \left(\frac{\rho_g Y_{g,6}}{W_6}\right)\left(\frac{\rho_g Y_{g,9}}{W_9}\right) \tag{18}$$

Gas-Phase Region

The species evolved from the propellant surface into the gas phase include vapor HMX, decomposition products of HMX and GAP, and unreacted GAP. Because condensed and gaseous species both exist in this region, a two-phase treatment similar to that described in the preceding section is employed to formulate the problem. The effect of laser absorption in the gas phase on the ignition and combustion processes of nitramine monopropellants has been extensively investigated in Ref. 11. Results indicate that only vapor RDX may absorb an appreciable amount of CO$_2$ laser energy in the gas phase. None of the major gaseous decomposition products of RDX exhibits a noticeable absorption at a wavelength of 10.6 μm of CO$_2$ laser. Thus, the fraction of the laser energy absorbed in the gas phase appears quite limited (less than 10%). The heat release from exothermic reactions is much more pronounced than the laser energy absorbed by the gas phase. The same argument applies to HMX as well since the decomposition species of HMX and RDX are similar

With the assumption that body force, viscous dissipation, and radiation emission/absorption effects are ignored, the isobaric conservation equations for both the condensed and gas phases can be combined and written as follows.

Mass

$$\frac{\partial[(1 - \phi_g)\,A\rho_c + \phi_g A\rho_g]}{\partial t} + \frac{\partial}{\partial x}[(1 - \phi_g)\,A\rho_c u_c + \phi_g A\rho_g u_g] = 0, \tag{19}$$

Condensed species concentration

$$\frac{\partial[(1 - \phi_g)\,A\rho_c Y_{c_i}]}{\partial t} + \frac{\partial}{\partial x}[(1 - \phi_g)\,A\rho_c u_c Y_{c_i}] = A\dot{w}_{c_i} \quad (i = 1,2, \ldots, N_c), \tag{20}$$

Gaseous species concentration

$$\phi_g A\rho_g \frac{\partial Y_{g_i}}{\partial t} + \phi_g A\rho_g u_g \frac{\partial Y_{g_i}}{\partial x} + \frac{\partial(\phi_g A\rho_g V_{g_i} Y_{g_i})}{\partial x} = A\dot{w}_{g_i} - Y_{g_i} A\dot{w}_{c\text{-}g} \quad (i = 1,2, \ldots, N_g), \tag{21}$$

Energy

$$\rho c_p A \frac{\partial T_g}{\partial t} - \frac{\partial (pA)}{\partial t} + \rho u c_p A \frac{\partial T_g}{\partial x} = \frac{\partial}{\partial x}\left(\lambda A \frac{\partial T_g}{\partial x}\right)$$
$$- \phi_g A \sum_{j=1}^{N_g} \rho_g Y_{g_i} V_{g_i} c_{p_{g_i}} \frac{\partial T_g}{\partial x} - A \sum_{j=1}^{N_g} \dot{w}_{g_j} h_{gj}$$
$$- A \sum_{j=1}^{N_c} \dot{w}_{cj} h_{cj} + A \sum_{j=1}^{N_g} h_{gj} Y_{gj} \dot{w}_{c-g} - A \sum_{j=1}^{N_c} h_{cj} Y_{cj} \dot{w}_{c-g}, \tag{22}$$

The thermophysical properties used in Eq. 22 are mass-averaged as follows.

$$\rho c_p = (1 - \phi_g)\, \rho_c c_c + \phi_g \rho_g c_g, \tag{23}$$

$$\rho u c_p = (1 - \phi_g)\, \rho_c u_c c_c + \phi_g \rho_g u_g c_g, \tag{24}$$

$$\lambda_g = [(1 - \phi_g)\, \rho_c u_c \lambda_c + \phi_g \rho_g u_g \lambda_g] / [(1 - \phi_g) \rho_c u_c] + \phi_g \rho_g u_g] \tag{25}$$

The enthalpy of gaseous or condensed species i in Eq. 22 is defined as

$$h_i = \int_{T_{ref}}^{T} c_{p_i} dT + h^{\circ}_{f_i} \tag{26}$$

The mass diffusion velocity V_i consists of contributions from both concentration and temperature gradients,

$$V_i = -D_i \frac{1}{X_i} \frac{\partial X_i}{\partial x} + D_i \frac{D_{T_i}}{X_i} \frac{1}{T} \frac{\partial T}{\partial x} \tag{27}$$

Finally, the equation of state for a multi-component system is used to close the formulation.

$$p = \rho_g R_u T_g \sum_{i=1}^{N_g} \frac{Y_{g_i}}{W_{g_i}} \tag{28}$$

The chemical reactions can be written in the following general form

$$\sum_{i=1}^{N_g} v'_{ij} M_i \underset{k_{bj}}{\overset{k_{fj}}{\Leftrightarrow}} \sum_{i=1}^{N_g} v''_{ij} M_i, \quad j = 1,2, \ldots, N_R \tag{29}$$

where v'_{ij} and v'_{ij} are the stoichiometric coefficients for the ith species appearing as a reactant in the jth forward and backward reactions, respectively, and M_i is the chemical symbol for the ith species. The reaction rate constant k_j (either k_{fj} or k_{bj}) is given by the Arrhenius expression

$$k_j = A_j T^{B_j} \exp(-E_j / R_u T) \tag{30}$$

The rate of change of molar concentration of species i by reaction j is

$$\dot{C}_{ij} = (v'_{ij} - v''_{ij}) \left(k_{fj} \prod_{i=1}^{N_g} C_i^{v'_{ij}} - k_{bj} \prod_{i=1}^{N_g} C_i^{v''_{ij}} \right) \tag{31}$$

The total mass production rate of gaseous species i in Eq. 21 is then obtained by summing up the changes due to all gas- and condensed-phase reactions:

$$\dot{w}_{g_i} = \phi_g W_{g_i} \sum_{j=1}^{N_R} \dot{C}_{ij} + \dot{w}_{c-g,g_i} \tag{32}$$

where $\dot{w}_{c-g,gi}$ represents the mass conversion rate from liquid to gas of gaseous species i.

The gas-phase chemical kinetics scheme is composed of four submodels: 1) the HMX combustion mechanism [9]; 2) the additional reactions, recently proposed by Chakraborty and Lin [32], involving the consumption of H_2CNNO_2, H_2CNNO, H_2CNO, and H_2CNOH, and H_2CN; 3) the initial decomposition reactions of GAP including, among others, aldehydes and imines; and 4) the hydrocarbon combustion mechanism [33] containing 49 species and 279 reactions. Bimolecular decomposition reactions for the aldehydes (CH_3CHO and C_2H_3CHO) and imines (CH_3CHNH and $CH_2CHCHNH$) are assumed, and their kinetic rates are estimated, as indicated by reactions (R7–R10) in Table 2. In total, the gas-phase chemical kinetics scheme involves 74 species and 532 reactions.

The mass production rates of species generated by condensed-phase reactions in Eqs. 20 and 21 are described by reactions (R3) and (R4) of condensed species such as GAP and its intermediate product. Thus, the rate expressions of reactions listed in Table 3, except (R1), (R2), (R5), and (R6), are utilized to calculate the mass production rates of species generated from GAP decomposition.

Boundary Conditions

The physical processes in the gas phase and foam layer must be matched at the propellant surface to provide the boundary conditions for each region. This procedure requires balances of mass and energy, and eventually determines propellant surface conditions and burning rate. With the neglect of mass diffusion in the condensed phase, the conservation laws at the propellant surface can be written as follows.

Mass

$$[(1-\phi_f)\rho_c u_c + \phi_f \rho_g u_g]_{0^-} = [(1-\phi_g)\rho_c u_c + \phi_g \rho_g u_g]_{0^+} \tag{33}$$

Species

$$[(1-\phi_f)\rho_c u_c Y_{c_i} + \phi_f \rho_g u_g Y_{g_i}]_{0^-} = [(1-\phi_g)\rho_c u_c Y_{c_i} + \phi_g \rho_g (u_g + V_{g_i}) Y_{g_i}]_{0^+} \tag{34}$$

Energy

$$\left[\lambda_f \frac{dT_f}{dx} + (1-\phi_f)\rho_c u_c Y_{\mathrm{HMX}_c} h_{\mathrm{HMX}_{l\to g}}\right]_{0^-} = \left[\lambda_g \frac{dT_g}{dx}\right]_{0^+} + \dot{Q}''_{laser} \tag{35}$$

The temperature is identical on both sides of the interface, but the void fraction and species mass fractions might be different. The treatment of surface absorption of incident radiative energy, Q''_{laser} is given in Ref. 11.

Because the propellant surface is defined as the interface where rapid phase transition occurs, the evaporation law of HMX is assumed to prevail at the interface [5], giving

$$[(1-\phi_f)\rho_c u_c Y_{\mathrm{HMX}_c}]_{0^-} = \left[s\bar{v}_n C_{\mathrm{HMX}_g}\left(\frac{p_{v,eq}}{p} - X_{\mathrm{HMX}_g}\right)\right]_{0^+} \tag{36}$$

Most of the existing data regarding HMX vapor pressure, as shown in Fig. 4, is based on the sublimation of HMX. The data obtained by Taylor and Crookes [34] is chosen in the present work because it results in reasonable predictions of propellant surface temperature and burning behavior.

It has been shown that $\rho_c u_c = \rho_g u_g$ is a good assumption for the two-phase model [5]. Equation 33 becomes trivial and Eq. 34 can be written as follows.

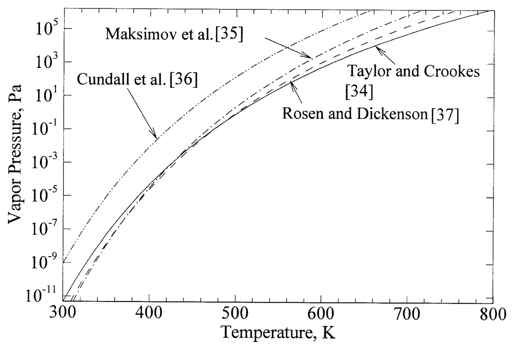

Fig. 4. Vapor pressure of HMX.

$$[(1-\phi_f)Y_{c_i} + \phi_f Y_{g_i}]_{0^-} = \left[(1-\phi_g)Y_{c_i} + \phi_g\left(1+\frac{V_{g_i}}{u_g}\right)Y_{g_i}\right]_{O^+} \tag{37}$$

A summation of the above equations for all the condensed species $\mathrm{GAP}_{(l)}$, $\mathrm{GAP}^*_{(l)}$, and $\mathrm{C}_{(s)}$ gives

$$[(1-\phi_f)(1-Y_{RDX_c})]_{0^-} = [(1-\phi_g)]_{0^+} \tag{38}$$

Equations 35 through 38 are sufficient to solve the set of unknowns (u, T, Y_i, ϕ) at the propellant surface and provide the boundary conditions for the foam layer and gas phase.

The boundary conditions at the interface (melt front) between the solid phase and foam layer are

$$T_c = T_f = T_{\mathrm{melt}} \text{ and } \phi_f = 0 \quad \text{at } x = x_{\mathrm{melt}} \tag{39}$$

$$\left[\lambda_c \frac{dT_c}{dx} + \rho_c u_c Y_{\mathrm{HMX}} h_{\mathrm{HMX}_{s\to l}}\right]_{x_{\mathrm{melt}}^-} = \left[\lambda_f \frac{dT_f}{dx}\right]_{x_{\mathrm{melt}}^+} \tag{40}$$

The far-field conditions for the gas phase require the gradients of flow properties to be zero at $x = \infty$.

$$\frac{\partial \rho}{\partial x} = \frac{\partial u}{\partial x} = \frac{\partial Y_i}{\partial x} = \frac{\partial T}{\partial x} = 0 \text{ at } x = \infty \tag{41}$$

The condition at the cold boundary for the condensed phase $(x = -\infty)$ is

$$T_c = T_i \text{ as } x \rightarrow -\infty \tag{42}$$

where T_i is the pre-conditioned temperature of the propellant. The initial mass fractions of HMX and GAP are also provided as input parameters.

NUMERICAL METHOD

The theoretical formulation established in the current work requires a robust computational scheme due to the numerical stiffness caused by chemical reactions and transport processes. All the conservation equations and associated boundary conditions are coupled and solved by a double-iteration procedure which treats the propellant surface temperature T_s and burning rate r_b as eigenvalues. The procedure continues with T_s adjusted by an inner loop while r_b is corrected by the outer iteration. The conservation equations for the subsurface region are solved first and the resulting species concentrations at the surface are used as the boundary conditions for the gas-phase region through the interfacial matching conditions. The next step involves integration of the gas-phase conservation equations to provide the temperature and species-concentration profiles. The non-equilibrium evaporation Eq. 36 is then employed to check the convergence of T_s. If this is not successful, another inner iteration is repeated using an updated value of T_s. The outer iteration follows the same procedure as the inner loop, except that r_b is used as the eigenvalue to check the interfacial energy continuity, Eq. 35. Because only the burning rate and surface temperature, and not the interfacial species composition, are involved in the iterative procedure, the present algorithm performs quite well and significantly reduces the computational burden.

The conservation Eqs. 4 through 7 for the subsurface region are fully coupled. They are, however, solved by an uncoupled-iteration method. The method starts with an estimated temperature profile obtained by solving an inert energy equation, and then the conservation equations of mass and species concentrations are integrated using a fourth-order Runge-Kutta method. Equation 7 is subsequently solved with the newly obtained void fraction and species concentrations to obtain another temperature profile. Since the equations are solved separately, iteration is required to ensure a converged solution that satisfies all the conservation laws and boundary conditions.

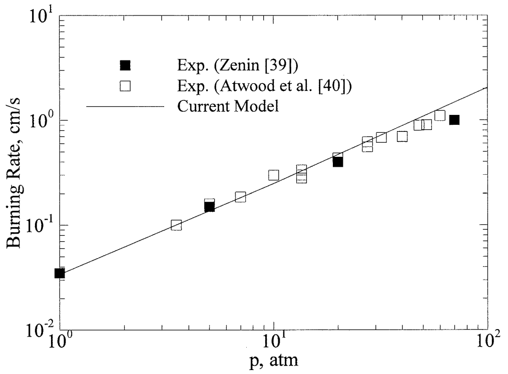

Fig. 5. Pressure dependence of burning rate of HMX monopropellant; self-sustained combustion.

The governing Eqs. 19 through 22 for the gas phase are fully coupled, but solved by an uncoupled-iteration method similar to the subsurface-region solver. Equation 20 is first solved using a fourth-order Runge-Kutta method to get the void fraction and the mass fractions of condensed species. Equations 19, 21, and 22 are then solved using the Chemkin-Premix [38] package with some modifications since the governing equations have been changed to account for a two-phase system. The grid systems of the two solvers are different and direct interpolation is used to match the grid information.

DISCUSSION OF RESULTS

The combustion characteristics of HMX monopropellant is first studied as a limiting case to validate the model. Figure 5 shows the pressure sensitivity of the HMX burning rate. Good agreement is obtained with the experimental measurements by Zenin [39] and Atwood et al. [40]. The pressure exponent n in the burning-rate law,

$$r_b = ap^n, \tag{43}$$

is about 0.88, with the pre-exponential factor a equal to 0.35 for $T_i = 293$ K. The temperature sensitivity of burning rate defined by Eq. 44 at various pressures is shown in Fig. 6.

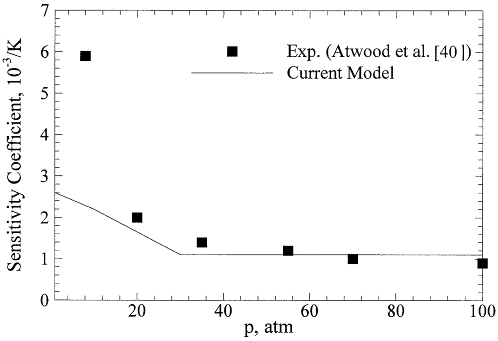

Fig. 6. Temperature sensitivity of burning rate of HMX monopropellant; self-sustained combustion.

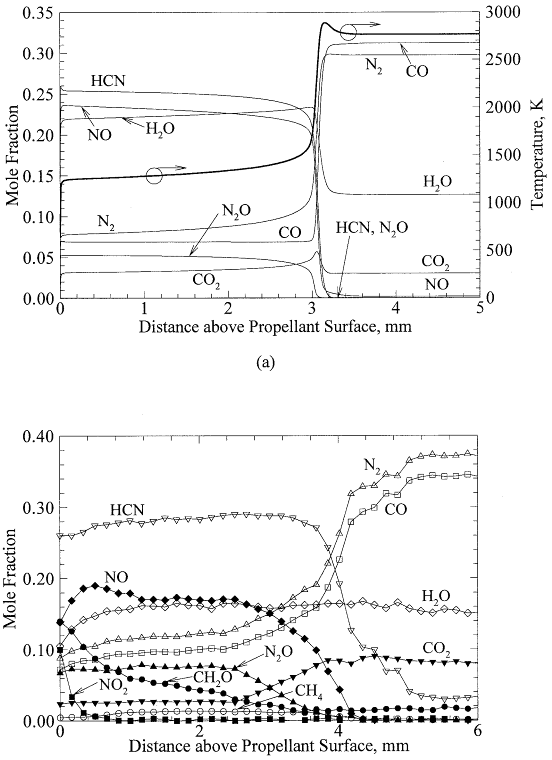

(a)

(b)

Fig. 7. (a) Calculated and (b) measured [3] species-concentration profiles of gas-phase flame of HMX/GAP pseudo propellant (mass ratio 8:2) at 1 atm and laser intensity of 100 W/cm^2.

$$\sigma_p = \left. \frac{\partial(\ln r_b)}{\partial T_i} \right|_p \tag{44}$$

There are discrepancies between the measured and predicted values at pressures below 20 atm, a phenomenon that may be attributed to the uncertainties in modeling the condensed-phase heat release process. More detailed understanding of the chemical kinetics in the condensed phase is required to improve model predictability, especially for low-pressure cases in which near-surface exothermic reactions play a more dominant role in determining propellant surface conditions than the heat feedback from the gas phase.

After validation, the analysis is applied to investigate HMX/GAP pseudo-propellant combustion over a broad range of pressure and laser intensity with various compositions. Figure 7 shows the temperature and species-concentration profiles in the gas phase at a CO_2 laser intensity of 100 W/cm^2 under atmospheric pressure. The ratio of HMX to GAP mass fraction is 8:2. Reasonable agreement was achieved with the experimental data reported in Ref. 3. The temperature rises rapidly from 677 K at the surface, levels off around 1200 to 1600 K, and further increases to its final value at 2780 K. The flame can be divided into three regions: 1) the primary flame, 2) the dark zone, and 3) the secondary flame. The dark zone is a nonluminous region between the primary and the secondary flame, and is characterized with a temperature plateau. Liau and Yang [41] indicated that the chemical preparation and fluid transport times of the intermediate species produced in the primary flame must be comparable to form a dark zone. The concentrations of HCN, NO, and H_2O in the dark zone appeared to be similar to those of pure nitramine propellants [3]. The rapid conversion of HCN and NO to N_2 and CO in the secondary flame zone were successfully predicted. The dominant net reactions in this stage are as follows.

$$2HCN + 2NO \Rightarrow 2CO + 2N_2 + H_2 \tag{R11}$$

$$N_2O + H_2 \Rightarrow N_2 + H_2O \tag{R12}$$

$$C_2N_2 + 2NO \Rightarrow 2CO + 2N_2 \tag{R13}$$

These reactions are highly exothermic and usually take place at high temperatures because of their large activation energies. The predicted flame stand-off distance of 3 mm is slightly shorter than the measured value of 4 mm, partly because of the ambiguity in defining the propellant surface during experiments.

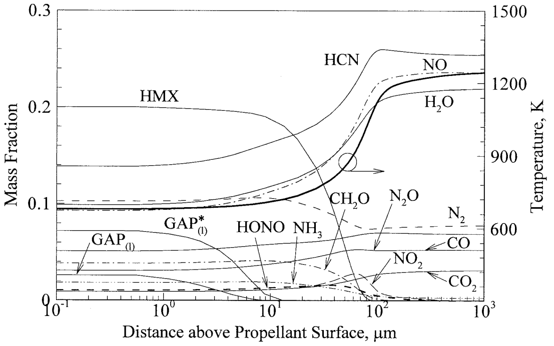

Fig. 8. Temperature and species-concentration profiles in near-surface region of HMX/GAP pseudo propellant (mass ratio 8:2) combustion at 1 atm and laser intensity 100 W/cm^2.

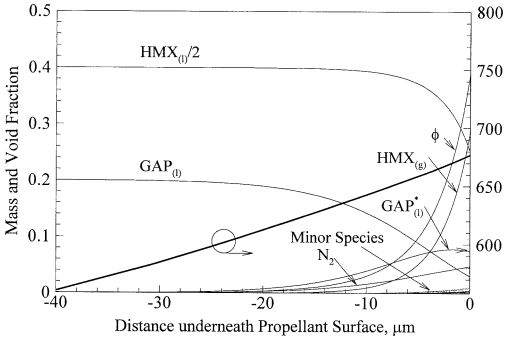

Fig. 9. Temperature and species-concentration profiles in subsurface of HMX/GAP pseudo propellant (mass ratio 8:2) combustion at 1 atm and laser intensity of 100 W/cm^2.

Figure 8 shows a close-up view of the primary flame immediately above the propellant surface, which extends over a length of 100 μm. The dominant reactions in this oxidation stage are R1, R2, and R6. The prediction of N_2O concentration was satisfactory compared with the measurement [3]; however, NO_2 and CH_2O appear to be consumed too fast. Intermediate reactions forming CH_2O and NO_2 are still lacking in the near-surface region to yield better agreement with experimental results. Conversion of GAP and GAP* to N_2, HCN, CO, NH_3, CH_2O, CH_3CHO, H_2O, C_2H_3CHO, C_2H_4, CH_3CHNH, and $CH_2CHCHNH$ occurs in a very short distance (~10 μm). The GAP decomposition is a highly exothermic process releasing a significant amount of energy in the gas phase. However, at the same time, the heat feedback from the gas phase to the surface is reduced due to the dilution of reactive species by the GAP pyrolysis gases. The decomposed fuel fragments, such as CH_2CHO, C_2H_3CHO, CH_3CHNH, and $CH_2CHCHNH$, further react to form CH_3, HCO, C_2H_3, and H_2CN, as listed in Table 2.

The species-concentration and temperature profiles in the foam layer are shown in Fig. 9. An appreciable amount of HMX evaporates to form gas bubbles in this region, but the extent of decomposition through the pathways (R1) and (R2) appears to be limited. On the other hand, most of the GAP compound is consumed to become GAP* and N_2, releasing heat to support pyrolysis in the condensed phase. Further decomposition of GAP* according to (R4), however, is constrained as a result of the low temperature condition. The predicted surface temperature and foam-layer thickness are 677 K and 30 μm, respectively.

At present, uncertainties still exist about the types of species formed and associated reaction rates for regions in close proximity to the burning surface. Much needs to be learned about the decomposition of HMX and GAP at conditions representative of propellant burning. In light of this, a parametric study on the effect of condensed-phase kinetics of HMX is performed using two different sets of rate constants available in the literature for (R1) and (R2) in Table 2, obtained respectively by Brill [27] from the T-jump/FTIR experiment and by Davidson and Beckstead [6] based on their combustion model. The reaction rates proposed by Brill are more than 50 times faster than those given in Ref. 6 over the temperature range studied. Figure 10 shows the comparison between the predicted burning rates, obtained using both sets of kinetics rates, and the measured data obtained by

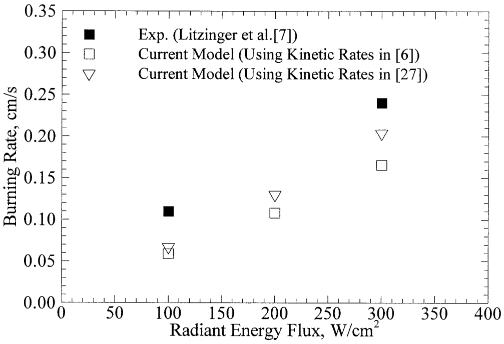

Fig. 10. Effect of condensed-phase kinetics on burning rate of HMX/GAP (mass ratio 8:2) at 1 atm.

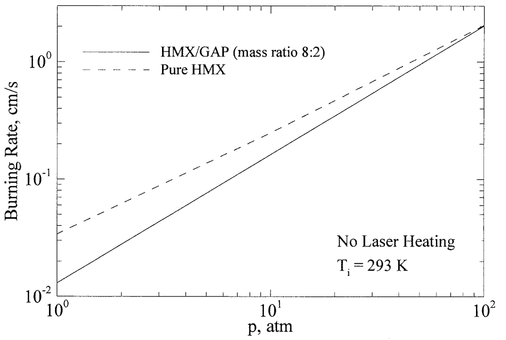

Fig. 11. Pressure dependence of burning rate of HMX/GAP pseudo propellant (mass ratio 8:2); self-sustained combustion.

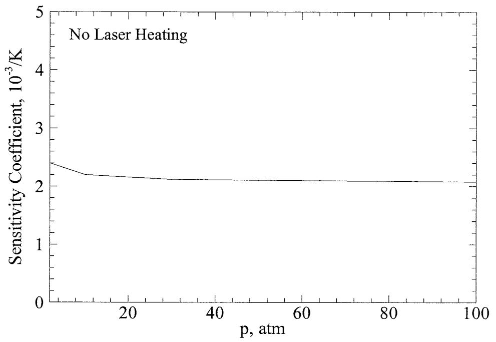

Fig. 12. Temperature sensitivity of burning rate of HMX/GAP pseudo propellant (mass ratio 8:2); self-sustained combustion.

Litzinger et al. [3], at laser intensities of 100 to 300 W/cm^2 under atmospheric pressure. The rates by Brill [27] give rise to higher burning rates than those by Davidson and Beckstead [6], but both models underpredict measured values. It should be noted that the initial void fractions of the HMX/GAP samples used in Ref. 3 are estimated to be about 9 to 12% by Parr [42]. The HMX had a crystal size of 75 μm, and the HMX/GAP mixture was not initially pressed at high pressure. These voids caused an increase in burning surface area, and significantly enhanced the burning rate when the flame moved down within the voids. Inconsistent experimental observations are reported in the current literature. In Litzinger's experiment using uncured propellants, the burning rates were increased with the addition of GAP under CO_2 laser fluxes [3], whereas Kubota and Sonobe [17] observed an opposite trend for self-sustained combustion of cured HMX/GAP propellants. The latter also found that the burning rate of HMX/GAP could be increased considerably by adding 2% lead citrate (PbCi) and 0.6% carbon (C). The HMX used in their experiment had a bimodal particle size distribution (i.e., 70% of 2 μm and 30% of 20 μm).

The calculated burning rate of HMX/GAP pseudo-propellant (mass ratio 8:2) over a pressure range of 1–100 atm without external laser heating is shown in Fig. 11. It is slightly lower than that of pure HMX for $p < 90$ atm, but the trend reverses for $p > 90$ atm. Figure 12 presents the corresponding temperature sensitivity of burning rate, which appears to be independent of pressure and has a value twice greater than that of pure HMX. In general, the effect of preconditioned temperature on propellant burning rate diminishes with increasing pressure and impressed laser intensity. The enhanced heat transfer to the propellant surface because of large energy release and reduced flame standoff distance in the gas phase at elevated pressure overrides the influence of preconditioned temperature in determining the energy balance at the surface, and consequently decreases the temperature sensitivity of burning rate.

Figure 13 shows the effect of propellant composition on burning rate at various pressures. The burning rate in general decreases with the addition of GAP, which releases a substantial amount of N_2 through the C-N_3 bond breaking in the near-surface region. Although the process is exothermic, the pressure of N_2 and large fuel fragments dilute the concentrations of surface reactive species, and consequently reduces the rate of energy release from HMX reactions.

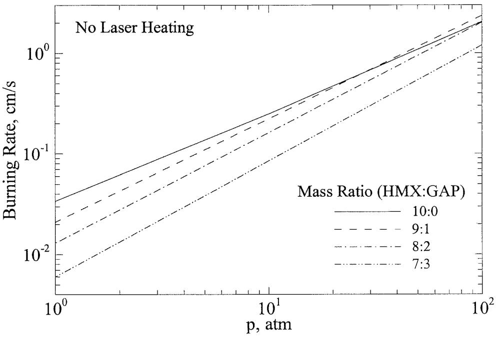

Fig. 13. Effect of propellant composition on burning rate at various pressures; self-sustained combustion.

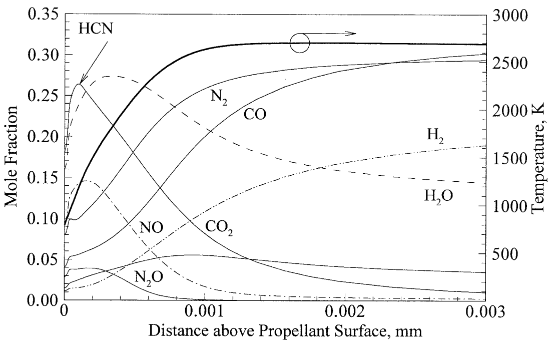

Fig. 14. Temperature and species-concentration profiles of gas-phase flame of HMX/GAP pseudo-propellant (mass ratio 8:2) at 100 atm and laser intensity of 100 W/cm^2.

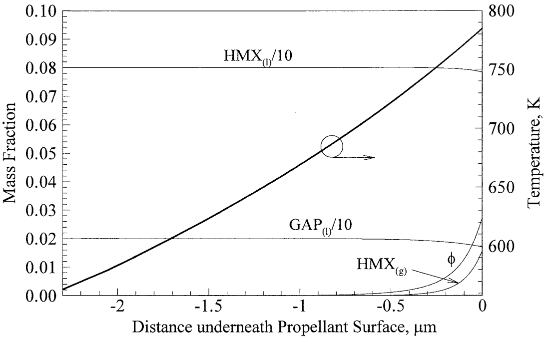

Fig. 16. Temperature and species-concentration profiles in subsurface region of HMX/GAP pseudo-propellant (mass ratio 8:2) combustion at 100 atm and laser intensity of 100 W/cm^2.

The heat feedback to the surface decreases accordingly, rendering a lower burning rate. Another factor contributing to this phenomenon is the blowing effect of the GAP compound, which tends to push the primary flame away from the surface. The situation is, however, different at high pressures. The burning rate of HMX/GAP pseudo-propellant with a mass ratio of 9:1 is greater than that of pure HMX for $p >$ 30 atm. To address this issue, we consider several competing processes controlling HMX/GAP combustion. Figures 14 through 19 present two sets of flame structures in various regimes for an HMX/GAP pseudo-propellant (mass ratio 8:2) and pure HMX, respectively, at $p = 100$ atm and laser intensity of 100 W/cm^2. The primary and secondary flames merge together for both cases at such a high pressure, with a monotonic increase of temperature from the surface to its final value. The thermal penetration layer in the condensed phase is extremely thin (on the order of 1 μm); no appreciable decomposition is observed because of the short residence time. The flame temperature of the HMX/GAP pseudo-propellant is considerably lower than that of pure HMX due to the large amount of inert and fuel species issuing from the GAP decomposition. Consequently, the heat feedback from the gas phase to the propellant surface decreases with the addition of GAP. On the other hand, the surface temperature increases considerably due to the presence of GAP (785 K vs. 712 K for pure HMX), to satisfy the thermodynamic requirement for HMX vapor pressure at the surface. This condition facilitates exothermic GAP decomposition, which then provides the energy to promote propellant burning. Other factors that may influence the surface temperature and burning rate are the thermophysical properties of GAP and HMX. The thermal conductivity of GAP is lower than that of HMX, as listed in Table 1, thereby yielding a higher surface temperature and burning rate. The transport properties of species in the near-surface region may also play an important role, but no succinct conclusion can be drawn because of the complexity of the mechanisms involved.

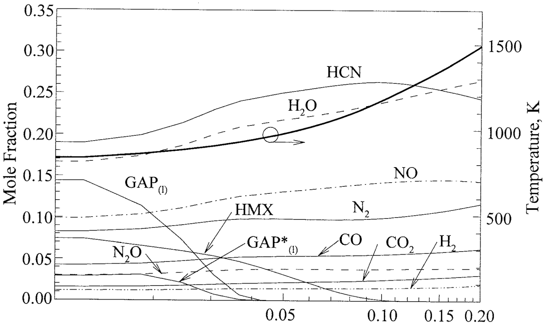

Fig. 15. Temperature and species-concentration profiles in near-surface region of HMX/GAP pseudo-propellant (mass ratio 8:2) combustion at 100 atm and laser intensity of 100 W/cm^2.

Although reasonably good agreement between the model prediction and experimental data reported in Ref. 3 was achieved in terms of the flame-standoff distance and overall combustion wave structure at 1 atm, as shown in Fig. 7, the discrepancy between the predicted flame-

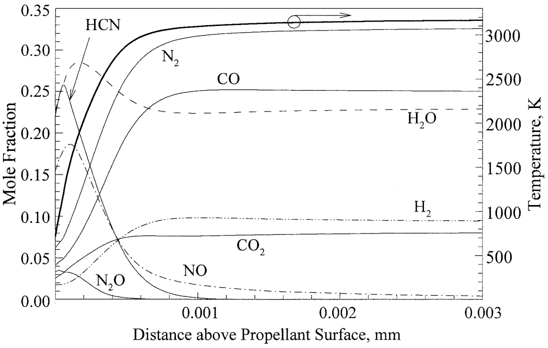

Fig. 17. Temperature and species-concentration profiles of gas-phase flame of pure HMX at 100 atm and laser intensity of 100 W/cm^2.

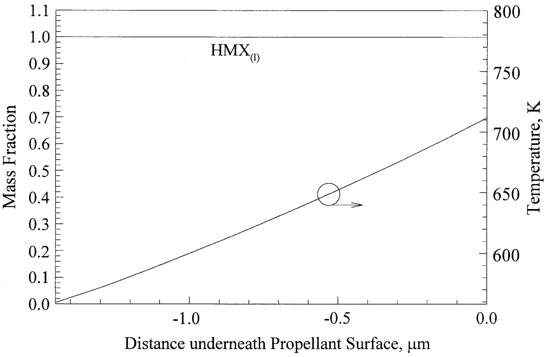

Fig. 19. Temperature and species-concentration profiles in subsurface region of pure HMX combustion at 100 atm and laser intensity of 100 W/cm^2.

standoff distance of pure HMX at high pressures (~100 atm) and measured data of Ref. 39 is evident. This may be attributed to the uncertainties associated with measurements and the effect of ambient conditions on experiments. For example, the current model treats propellant burning as a one-dimensional, adiabatic combustion process. The calculated flame temperature thus becomes much higher than the measured value in a strand burner environment in which the heat loss to the ambience is significant. The discrepancy may also result from the lack of calibrated thermochemical properties for high pressures. The chemical kinetics scheme and its associated parameters are basically established at low pressure cases. Extrapolation of these results to high-pressure conditions naturally gives rise to uncertainties and requires future studies. Nonetheless, the current model provides detailed insight into the key physiochemical processes involved in the steady-state combustion of nitramine/azide pseudo-propellants and can serve as a framework for further improvement of propellant combustion modeling.

Figures 20 and 21 show the effect of laser intensity on burning rate for several mixture ratios at 10 and 100 atm, respectively. At 10 atm, the burning rate increases with increasing CO_2 laser intensity. Although GAP decomposition is highly exothermic, the burning rate decreases with increasing GAP concentration since the fuel-rich pyrolysis products of GAP reduce the flame temperature and move the flame away from the surface. At a high pressure of 100 atm, the intensive heat transfer from the flame to the surface overrides the effect of surface radiant energy absorption. The burning rate thus appears to be insensitive to the impressed laser intensity. The influence of GAP concentration on burning rate exhibits a differ-

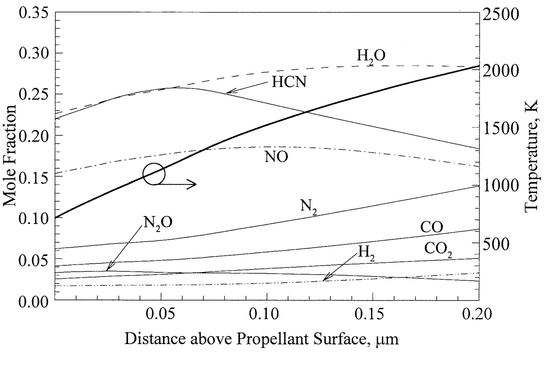

Fig. 18. Temperature and species-concentration profiles in near-surface region of pure HMX combustion at 100 atm and laser intensity of 100 W/cm^2.

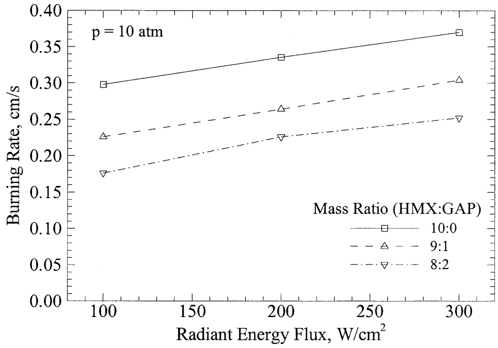

Fig. 20. Effect of propellant composition on burning rate at various CO_2 laser intensities; $p = 10$ atm.

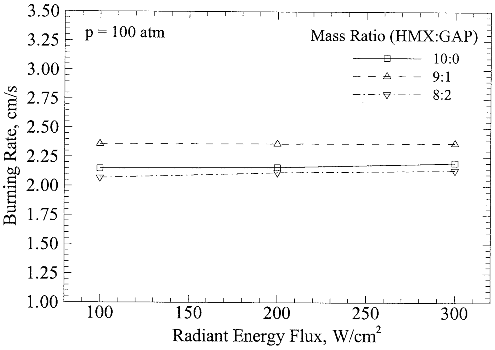

Fig. 21. Effect of propellant composition on burning rate at various CO_2 laser intensities; $p = 100$ atm.

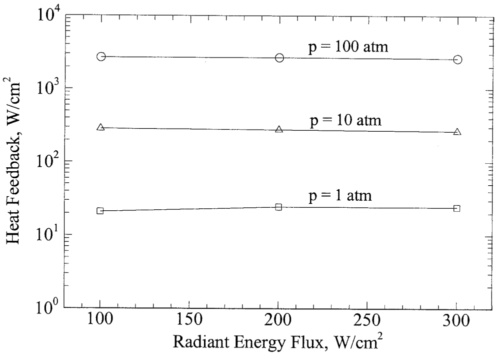

Fig. 23. Heat feedback to propellant surface at various CO_2 laser intensities and pressures (HMX/GAP mass ratio 8:2).

ent trend from that at 10 atm due to the variation of surface temperature, a phenomenon that has been elaborated in connection with the discussion of Fig. 13.

The effects of laser heat flux and pressure on the burning rate of HMX/GAP pseudo-propellant (mass ratio 8:2) are shown in Fig. 22. The impressed laser flux causes a substantial increase in burning rate at low pressures (e.g., 1 and 10 atm). The effect, however, diminishes at high pressure, because the heat feedback from the gas phase overshadows the surface laser absorption in determining the energy balance at the surface, as shown in Fig. 23. The heat transfer to the burning surface increases almost linearly with pressure. Figure 24 shows the propellant surface temperature as a function of radiant heat flux at several pressures. The trend resembles that for the burning rate shown in Fig. 22. The melt-layer thickness and surface void fraction are shown in Figs. 25 and 26, respectively. They both decrease with increasing radiant heat flux at low pressure, but remain almost fixed at high pressure. It should be noted that the bubble formation rate can be enhanced with increasing temperature, but may also be reduced by the decreased residence time resulting from the increased burning rate at high temperature. The present case shows a net decrease in the surface void fraction with increasing pressure.

CONCLUDING REMARKS

A numerical analysis has been developed to study the key physiochemical processes involved in the combustion of HMX/GAP pseudo-propellant. The formulation is based on the conservation equations of mass, energy, and species for both the condensed and gas phases, and takes into account finite-rate chemical kinetics and variable thermophysical properties. The model has been applied to a broad range of

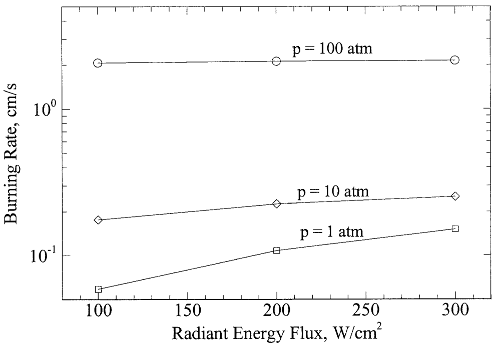

Fig. 22. Effect of pressure on burning rate at various CO_2 laser intensities (HMX/GAP mass ratio 8:2).

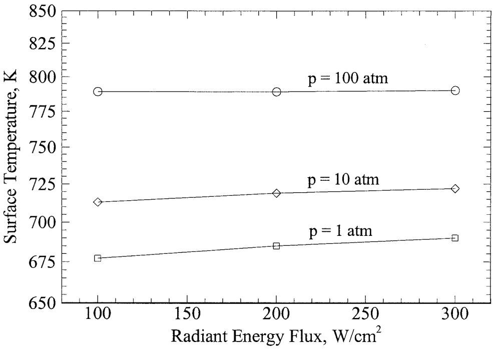

Fig. 24. Effect of CO_2 laser intensity on surface temperature at various pressures (HMX/GAP mass ratio 8:2).

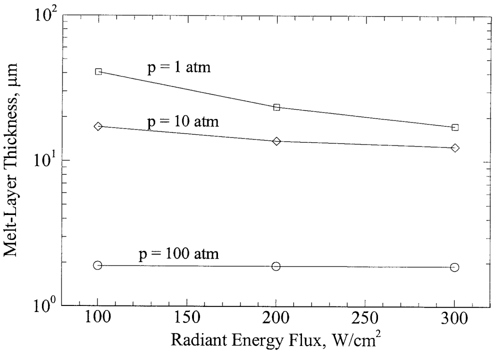

Fig. 25. Effect of CO_2 laser intensity on melt-layer thickness at various pressures (HMX/GAP mass ratio 8:2).

pressure, laser intensity, and propellant composition. Reasonably good agreement is achieved between the predicted and measured species concentration profiles at a laser intensity of 100 W/cm^2 under atmospheric pressure. At low pressures, the laser heat flux has a strong effect on the combustion wave structure and burning characteristics of propellants. The influence, however, diminishes at high pressures since the conductive heat feedback from the gas to the condensed phase overrides the laser energy absorption in determining the propellant surface condition. The addition of GAP decreases the burning rate at low pressures, even though the burning rate of GAP itself is higher than that of pure HMX. Conversely, above certain pressure levels, the burning rate may be considerably enhanced by adding a small amount of GAP.

It is evident that more experimental data, such as burning rate, temperature and species-concentration profiles under various conditions are needed for further model validation. The condensed-phase and near-surface kinetics of HMX and GAP still remains as an essential part of the overall effort to achieve a comprehensive understanding of HMX/GAP pseudo-propellant combustion. The flame expansion has not been taken account in the current model due to the uncertainties as to how the rapid gas expansion occurs in the flame zone. The lack of reliable thermophysical properties poses another limitation in model accuracy. Nonetheless, the present study provides a general framework for studying the key physiochemical processes involved in the combustion of nitramine/azide pseudo-propellants.

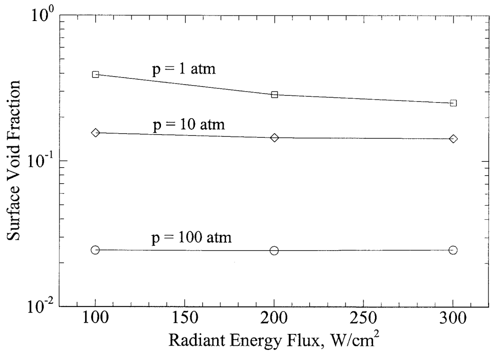

Fig. 26. Effect of CO_2 laser intensity on surface void fraction at various pressures (HMX/GAP mass ratio 8:2).

This work was sponsored partly by The Pennsylvania State University and partly by the California Institute of Technology Multidisciplinary University Research Initiative under ONR Grant No. N00014-95-1-1338.

REFERENCES

1. Parr, T. P., and Hanson-Parr, D. M., in *Solid Propellant Chemistry, Combustion, and Motor Interior Ballistics*, (V. Yang, T. B. Brill, and W. Z., Ren, Eds.), Vol. 185, Progress in Astronautics and Aeronautics, AIAA, Reston, VA, 2000, pp. 381–411.
2. Korobeinichev, O. P., in *Solid Propellant Chemistry, Combustion, and Motor Interior Ballistics*, (V. Yang, T. B. Brill, and W. Z., Ren, Eds.), Vol. 185, Progress in Astronautics and Aeronautics, AIAA, Reston, VA, 2000, pp. 335–354.
3. Litzinger, T. A., Lee, Y.-J., and Tang, C.-J., in *Solid Propellant Chemistry, Combustion, and Motor Interior Ballistics*, (V. Yang, T. B. Brill, and W. Z., Ren, Eds.), Vol. 185, Progress in Astronautics and Aeronautics, AIAA, Reston, VA, 2000, pp. 355–379.
4. Melius, C. F., in *Chemistry and Physics of Energetic Materials* (S. Bulusu, Ed.), Kluwer Academic, Norwell, MA, 1990, pp.21–78.
5. Liau, Y.-C., and Yang, V., *J. Prop. Power*, 11:727–739 (1995).
6. Davidson, J. E., and Beckstead, M. W., *Twenty-Sixth Symposium (International) on Combustion*, The Combustion Institute, Pittsburgh, 1996, pp. 1989–1996.
7. Davidson, J. E., and Beckstead, M. W., *J. Prop. Power* 13:375–383 (1997).
8. Prasad, K., Yetter, R. A., and Smooke, M., *Combust. Sci. Technol.* 124:35–82 (1997).
9. Prasad, K., Yetter, R. A., and Smooke, M., *Combust. Flame* 115:406–416 (1998).
10. Miller, M. S., and Anderson, W. R., in *Solid Propellant Chemistry, Combustion, and Motor Interior Ballistics*,

(V. Yang, T. B. Brill, and W. Z., Ren, Eds.), Vol. 185, Progress in Astronautics and Aeronautics, AIAA, Reston, VA, 2000, pp. 501–531.

11. Liau, Y.-C., Kim, E. S., and Yang, V., *Combust. Flames* 126:1680–1698 (2001).
12. Yang, V., Brill, T. B., and Ren, W. Z. (Eds.), *Solid Propellant Chemistry, Combustion, and Motor Interior Ballistics*, Vol. 185, Progress in Astronautics and Aeronautics, AIAA, Reston, VA, 2000, 990 pages.
13. Liau, Y.-C., Yang, V., and Thynell, S. T., in *Solid Propellant Chemistry, Combustion, and Motor Interior Ballistics*, (V. Yang, T. B. Brill, and W. Z., Ren, Eds.), Vol. 185, Progress in Astronautics and Aeronautics, AIAA, Reston, VA, 2000, pp. 477–500.
14. Puduppakkiam, K., and Beckstead, M. W., *Proceedings of Thirty-seventh JANNAF Combustion Subcommittee Meeting*, CPIA Publ, Chemical Propul Information Agency, John Hopkins University, Columbia, MD, 2000.
15. Faber, M., Harris, S. P., and Srivastava, R. D., *Combust. Flame* 55:203–211 (1984).
16. Flanagan, J.E., Woolery, D.O., and Kistner, R.L., AFAL-TR-87-107, Air Force Astronautics Laboratory, Edwards AFB, CA, 1987.
17. Kubota, N., and Sonobe, T., *Twenty-Third Symposium (International) on Combustion*, 1990, pp. 1331–1337.
18. Lengellé, G., Fourest, B., Godon, J.C., and Guin, C., AIAA Paper 93-2413 (1993).
19. Arisawa, H., and Brill, T. B., *Combust. Flame* 112:533–544 (1998).
20. Tang, C.-J., Lee, Y., and Litzinger, T. A., *Combust. Flame* 117:244–256 (1999).
21. Zenin, A. A., and Finjakov, S. V., AIAA Paper 2000-1032 (2000).
22. Kim, E. S., The Pennsylvania State University, Department of Mechanical and Nuclear Engineering, Ph.D. Thesis, 2000.
23. Hanson-Parr, D. M., and Parr, T. P., *J. Energetic Materials* 17:1–47 (1999).
24. Li, S. C., Williams, F. A., and Magolis, S. B., *Combust. Flame* 80:329–349 (1990).
25. Maksimov, Yu. Ya., *Zhur. Fiz. Khim.* 66:540–542 (1992).
26. Hall, P. G., *Trans. Faraday Soc.* 67:556–562 (1971).
27. Brill, T. B., *J. Prop. Power* 11:740–751 (1995).
28. Lin, C.-Y., Wang, H.-T., Lin, M. C., and Melius, C. F., *Int. J. Chemical Kinetics* 22:455– 482 (1990).
29. Sysak, G. S., Kim, E. S., and Thynell, S. T., *Proceedings of Thirty-Fifth JANNAF Combustion Meeting*, Tucson, AZ, December 7–11, 1998.
30. Oyumi, Y., and Brill, T. B., *Combust. Flame* 65:127–135 (1986).
31. Chen, J. K., and Brill, T. B., *Combust. Flame* 87:157–168 (1991).
32. Chakraboty, D., and Lin, M. C., in *Solid Propellant Chemistry, Combustion, and Motor Interior Ballistics*, (V. Yang, T. B. Brill, and W. Z., Ren, Eds.), Vol. 185, Progress in Astronautics and Aeronautics, AIAA, Reston, VA, 2000, pp. 33–71.
33. Frenklach, M., Bowman, T., Smith, G., and Gardiner, B., "GRI-MECH 1.2," Downloaded from http://euler.berkeley.edu/gri_mech/index.html.
34. Taylor, J. W., and Crookes, R. J., *J. Chemical Society, Faraday Trans. I* 72:723–729 (1976).
35. Maksimov, Yu. Ya., Apal'kova, V. N., Braverman, O. V., and Solov'ev, A. I., *Russian J. Phys. Chem.* 59:201–204 (1985).
36. Cundall, R. B., Palmer, T. F., and Wood, C. E. C., *J. Chemical Society, Faraday Trans. I* 74:1339–1345 (1978).
37. Rosen, J. M., and Dickenson, C., *J. Chem. Engineering Data* 14:120–124 (1969).
38. Kee, R. J., Grcar, J. F., Smooke, M. D., and Miller, J. A., *A Fortran Program for Modeling Steady, Laminar, One-Dimensional, Premixed Flames*, Sandia Report SAND85–8240, Sandia National Laboratories, Albuquerque, NM, 1985.
39. Zenin, A., *J. Prop. Power* 11:752–758 (1995).
40. Atwood, A. I., Boggs, T. L., Curran, P. O., Parr, T. P., and Hanson-Parr, D. M., *J. Prop. Power* 15:740–752 (1999).
41. Liau, Y.-C., and Yang, V., AIAA Paper 97-0589, January 1997.
42. Parr, T., private communication, Naval Air Warfare Center Weapons Division, China Lake, CA, 2000.

Received 23 January 2002; revised 5 June 2002; accepted 13 June 2002